2023

Heat Release And Flame Scale Effects On Turbulence Dynamics In Confined Premixed Flows

Max Fortin
University of Central Florida

HEAT RELEASE AND FLAME SCALE EFFECTS ON TURBULENCE DYNAMICS IN CONFINED PREMIXED FLOWS

By

MAX FORTIN
B.S. College of Engineering and Computer Science, 2021

A thesis submitted in partial fulfillment of the requirements
for the degree of Master of Science
in the Department of Mechanical and Aerospace Engineering
in the College of Engineering and Computer Science
at the University of Central Florida
Orlando, Florida

Spring Term
2023

Major Professor: Kareem Ahmed

ABSTRACT

As industry transitions to a net-zero carbon future, turbulent premixed combustion will remain an integral process for power generating gas turbines and are also desired for aviation engines due to their ability to minimize pollutant emissions. However, accurately predicting the behavior of a turbulent reacting flow field remains a challenge. To better understand the dynamics of premixed reacting flows, this study experimentally investigates the evolution of turbulence in a high-speed bluff-body combustor. The combustor is operated across a range of equivalence ratios from 0.7-1 to quantify the role of heat release and flame scales on the evolution of turbulence as the flow evolves from reactants to products. High-speed particle image velocimetry and CH* chemiluminescence imaging systems are simultaneously employed to quantify turbulent flame and flow dynamics. The results demonstrate that the flame augments turbulence fluctuations as the flow evolves from reactants to products for all cases. However, turbulence fluctuations increase monotonically with the heat of combustion and corresponding turbulent flame speed. Nondimensional spatial profiles of turbulence are used to develop a correlation to predict the increase in turbulent fluctuations in an extended progress variable space. A Reynolds Averaged Navier Stokes (RANS) decomposition is also explored to better characterize the effects of heat release on turbulence evolution dynamics. The correlations and RANS decomposition can guide modeling capabilities to better predict confined turbulent reacting flows and accelerate design strategies for premixed turbines with carbon-free fuels.

TABLE OF CONTENTS

LIST OF FIGURES

LIST OF TABLES

CHAPTER ONE: INTRODUCTION

Premixed flame and turbulent flow field interaction is a complex phenomenon, where turbulence affects flame topology and chemical kinetics, and the exothermic heat release alters the flow field. This study is focused on the latter phenomenon, isolating the effects of exothermic heat release on the turbulent flow field. Chemical heat release will affect fluid transport properties such as density and viscosity, which ultimately alters turbulence length scales, time scales, and the energy cascade[1]. Although previous studies of turbulence evolution across a flame have been performed, more knowledge is desired with an emphasis on more practical and industry relevant conditions. Additionally, as hydrogen becomes a more prevalent fuel for power generation and aviation engines, further knowledge of confined turbulent reactions will guide the development of more robust modeling tools. Improved numerical modeling tools will allow for more efficient and economic development of carbon free turbine technologies.

Several numerical studies have investigated the evolution of turbulence across premixed flames [2–11]. However, most of these studies have been limited to small-scale, unconfined jet flames or flames subject to homogenous, isotropic turbulence in a box. The numerical studies show turbulence attenuation across the flame as the flow evolves from reactants to products. Most literature attributes this dampening to an increase in kinematic viscosity due to the temperature rise across the flame. The rise in kinematic viscosity will allow for viscous dissipation effects to dominate turbulent transport dynamics, thereby dampening turbulent kinetic energy across a flame. To expand on numerical studies, recent experiments have also been performed with highly turbulent, unconfined, piloted jet flames [12–14]. The experimental results support the numerical

studies, showing turbulence attenuation as the flow progresses from the reactants to the products. The large variety of burner configurations utilized in these studies suggests that the turbulence attenuation phenomenon is geometrically independent, and that trends should uphold in shear dominated flows for propulsion and power production.

However, a more recent experimental study [15] utilizing a swirl burner performed an enstrophy transport analysis across the premixed flame and concluded that the turbulent source term of baroclinic torque is significant relative to turbulent sink terms of enstrophy stretching and viscous dissipation. The key difference between this study and previous numerical and experimental work was the presence of a considerable mean pressure gradient in the flow field and suggests that the balance of turbulence source and sink terms is altered in practical, engine relevant flow fields. There have been additional recent studies of vorticity and enstrophy transport analysis in flow fields subjected to mean pressure gradients that also confirm the significance of the baroclinic torque source term [16–20]. The relationship between vorticity/enstrophy transport dynamics and turbulence evolution across premixed flames was expanded upon in a recent experimental study of a bluff-body flame in both a confined and unconfined set-up[20]. It was found that while the unconfined configuration experienced attenuated turbulence across the flame, the confined configuration experienced augmentation across the flame. This augmentation is due to the lack of flow expansion inherent to the confined configuration. This lack of expansion manifests in increased mean velocity and increased turbulent fluctuations. The increased fluctuations are coupled with an increase in baroclinic torque production due to the stronger streamwise pressure gradients experienced in confined flows. Ultimately, the recent works highlight a greater need for investigating premixed confined reacting flows and understanding how the dominating physics diverge from the unconfined knowledge base.

This study aims to expand upon recent work and quantify the effects of heat release and flame scales on turbulence evolution in confined, premixed flows. An experiment is conducted within a confined premixed bluff-body burner. The combustor utilized a range of equivalence ratios to alter heat of combustion, flame thickness, and flame speed. Quantifying the role of heat release and flame scales on turbulence dynamics will allow for further refinement of modeling tools, which can accelerate design and development efforts for reacting propulsion and power systems.

CHAPTER TWO: METHODOLOGY

The experimental study was performed in the high-speed methane-air combustion facility at the Propulsion and Energy Research Laboratory at the University of Central Florida. Simultaneous 20 kHz CH* chemiluminescence and Particle Image Velocimetry (PIV) were used to visualize the flame front and capture turbulent velocity fields, respectively. A range of equivalence ratios were explored to isolate the effects of heat release and flame scales on turbulence evolution. Details of the experimental facility, high-speed diagnostics, and testing conditions are provided below.

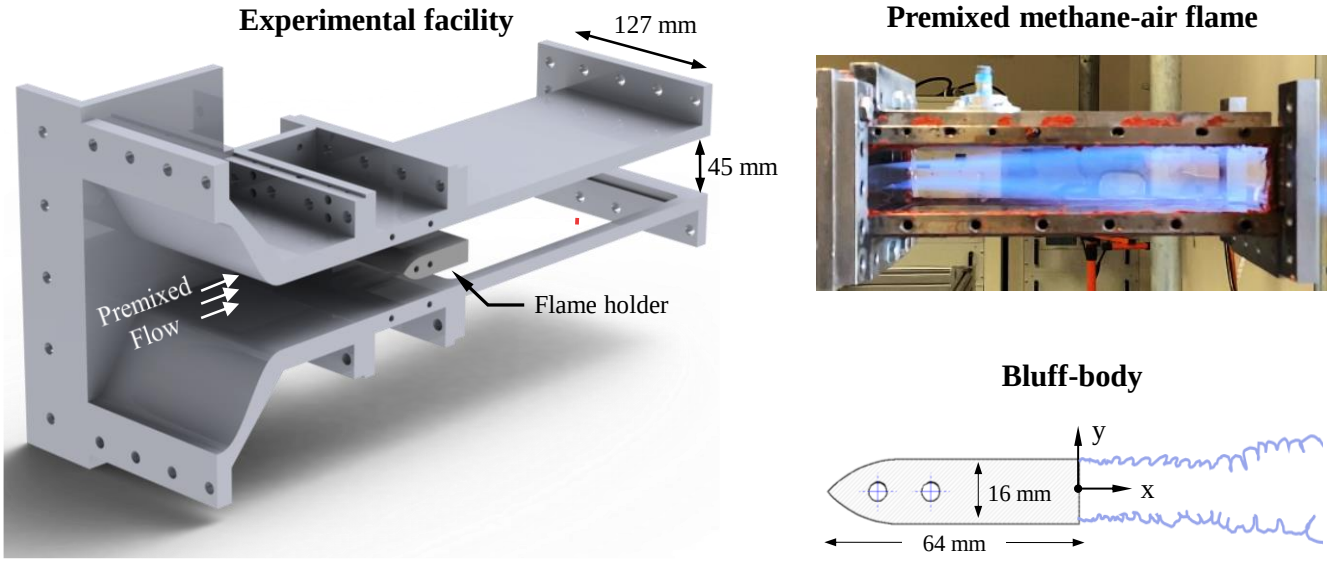

Figure 1: Experimental bluff-body facility, including a visual example of a premixed stabilized methane-air flame, the dimensions of the bluff-body, and the coordinate axis

2.1 Experimental Facility and Diagnostics

Figure 1 shows an overview of the experimental facility, which consists of a nozzle, flame holder, and an optically accessible viewing section. Methane (CH4) and air are injected far upstream (> 2 m) of the nozzle and conditioned through a mixing plenum [17,21,22]. Downstream of the nozzle is a bluff body flame holder with a length of 64 mm and a height of 16 mm, resulting in a blockage ratio of 36%. The flow is imaged through an optically accessible test section with the dimensions 220 x 45 x 127 mm (length, height, and width, respectively). The bottom and side walls are optically accessible through fused quartz windows which provide 95% transmissibility for wavelengths between 250 – 700 nm. The top wall is the only one that does not permit optical access and is coated in a nonreflective black paint to prevent light reflections.

The air and fuel delivery systems are independently controlled to fine tune upstream mass flows to obtain the desired test conditions. The air system is supplied upstream from high pressure tanks and metered with a Tescom dome style regulator and Fisher electro-pneumatic valve. Downstream of the valve, the air pressure is measured using a Dwyer pressure transducer before being choked through a 5/16" (~8mm) restriction orifice union. The discharge coefficient was calculated using a Coriolis flowmeter with a 2% accuracy, and the transducer measurement accuracy is ±0.75 psi. Combining both uncertainties and performing a propagation of error results in a total mass flow uncertainty of ± 0.6 g/s. The pressure measurements are fed into a custom LabView PID software which controls the electropneumatic valve's position to uphold a certain mass flow of air for the duration of the experiment. Methane is injected into the air stream, and the flowrate is controlled utilizing a pressure regulator, inline orifice, and solenoid valve.

The flame and flow field were investigated with simultaneous 20 kHz particle image velocimetry (PIV) and 20 kHz CH* chemiluminescence. The PIV imaging utilized 3 μm aluminum oxide (Al2O3) tracer particles injected upstream of the test section using a pressurized air seeder. The Stokes number for this configuration was determined to be St = 0.017[20]. Mie scattering of the particles is achieved using a 523 nm, solid-state, ND:YAG laser (LDP-200MQG Dual) sequentially pulsed at 20 kHz. The optical set up consists of a 1000 mm focusing lens and a -12.7 mm focal length cylindrical lens to form a thin laser sheet. The laser sheet is directed into the test section with a mirror. The scattered light is collected with a high-speed CMOS camera (Photron SA-Z) equipped with a 70-300 mm focal length lens and a 532 nm filter. The camera image resolution is 1000 x 1024 pixels viewing a 78 x 80 mm domain (~80 microns/pixel). The resulting images are processed using PIVLab integrated within the MATLAB software. The images were processed with a multi-pass cross-correlation scheme. The initial interrogation box size for

processing was 64 x 64 pixels and reduced to a final box size of 16 x 16 pixels with a 50% overlap used for each pass. The resulting measurement resolution is 1.25 mm based on the final cross-correlation box size, and the vector resolution is $\lambda = 0.625$ mm based on the 50% overlap. The vector resolution corresponds to $\lambda/lf = 1.45$ where lf is the laminar flame thickness at an equivalence ratio of 1.0. The uncertainty in velocity vectors, based on correlation statistics, is approximately 1 m/s, which is 4% of the freestream velocity for all test conditions. To obtain flame front position, CH* chemiluminescence images are captured with a high-speed CMOS camera (Photron SA1.1) equipped with a 5 0mm, f/1.2 lens and a 430 nm filter. The resulting image size is 640 x 368 pixels viewing a domain of 102 x 59mm. The corresponding image resolution is 0.16 mm/pixel.

Flame front contours are extracted from both PIV and CH* chemiluminescence images. For this study, the PIV flame traces were ultimately used for analysis since the images provide a planar visualization of the flame front which resides in the same plane as the velocity vectors. The PIV flame front extractions were performed by identifying the interface of a sudden drop in seed density due to the flame heat release and has been used to obtain reliable flame front contours across a range of turbulence conditions [23–25]. The interface was found by performing three median filter operations, each with a 3 x 3 window size, to mitigate image noise. The image was then binarized about a statistical threshold determined using Otsu's method[26], and instantaneous flame front contours are extracted from the binarized images through a boundary detection algorithm[27]. The CH* chemiluminescence flame front was extracted using the same process described above. The mean flame front extracted from both methods was found to be nominally similar.

Table 1: Experimental Conditions

Φ	u'_{rms} (m/s)	l_f (mm)	s_l (cm/s)	u'_{rms}/s_l	l_0/l_f	Da	Ka	ΔH_c (kJ/s) · 10^5
0.7	0.64	0.69	16.2	3.95	10.87	3.52	1.64	8.02
0.8	0.53	0.55	24.6	2.60	13.64	4.79	1.30	7.22
0.9	0.75	0.49	32.2	1.99	15.31	4.93	1.40	6.42
1.0	0.64	0.43	37.4	1.71	17.44	10.19	0.54	5.62

2.2 Experimental Conditions

Table 1 shows the experimental test conditions. The mean freestream flow velocity and Reynolds number of the incoming reactants (u_∞, $Re = u_\infty H/\nu$) were held constant at 25 m/s and 23,500, respectively. The influence of heat release was isolated by varying the reactant equivalence ratio over a range of 0.7 to 1.0. The turbulent velocity fluctuations in the freestream reactants are calculated with Eqs. (1) and (2), integral length scales are calculated with Eq. (3), and the Damköhler and Karlovitz numbers are calculated with Eqs. (4) and (5) respectively. The laminar flame thickness is obtained from Lafay et al [28]. and laminar flame speed from Vageopolous et al. and Amirante et al [29,30].

$$\bar{u} = \frac{1}{N}\sum_{i=1}^{N} u(t_i) \tag{1}$$

$$u'_{rms} = \left[\frac{1}{N-1}\sum_{i=1}^{N}(u(t_i) - \bar{u})^2\right]^{\frac{1}{2}} \tag{2}$$

$$l_0 = \int_{y_{min}}^{y_{max}} \frac{u'(x,y_0)u'(x,y)}{u'(x,y_0)^2}\,dy \tag{3}$$

$$Da = \frac{l_0/u'_{rms}}{l_f/s_l} \tag{4}$$

$$Ka = \left(\frac{u'_{rms}}{s_l}\right)^{\frac{3}{2}}\left(\frac{l_f}{l_0}\right)^{\frac{1}{2}} \tag{5}$$

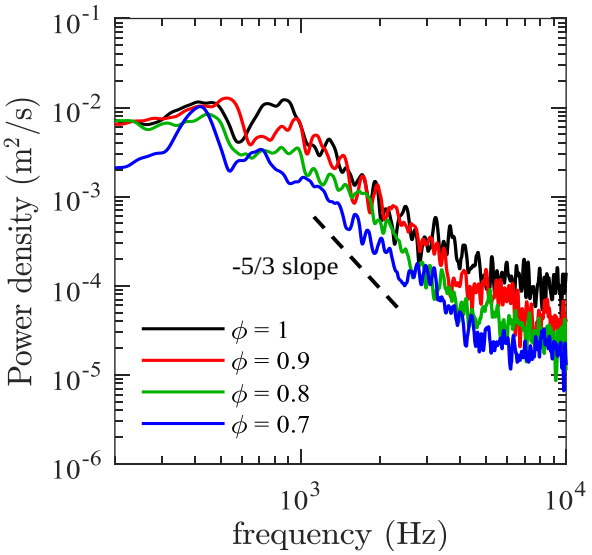

Figure 2: Spectra of the streamwise velocity in the freestream reactants

Figure 2 shows the turbulence spectra for the streamwise component of velocity in the freestream reactant region. The spectra are obtained using the Welch method [31] , which provides a Fourier transform based method to obtain a power spectrum of the time resolved velocity. Spectral curves are calculated through the reactant regions of the domain, and an ensemble average of the spectral curves obtained from the reactant region is presented in Fig. 2. The turbulence spectra for the reactant flow are nominally similar between all test cases and depicts a Kolmogorov-type -5/3 decay slope.

CHAPTER THREE: RESULTS

3.1 Experimental Facility and Diagnostics

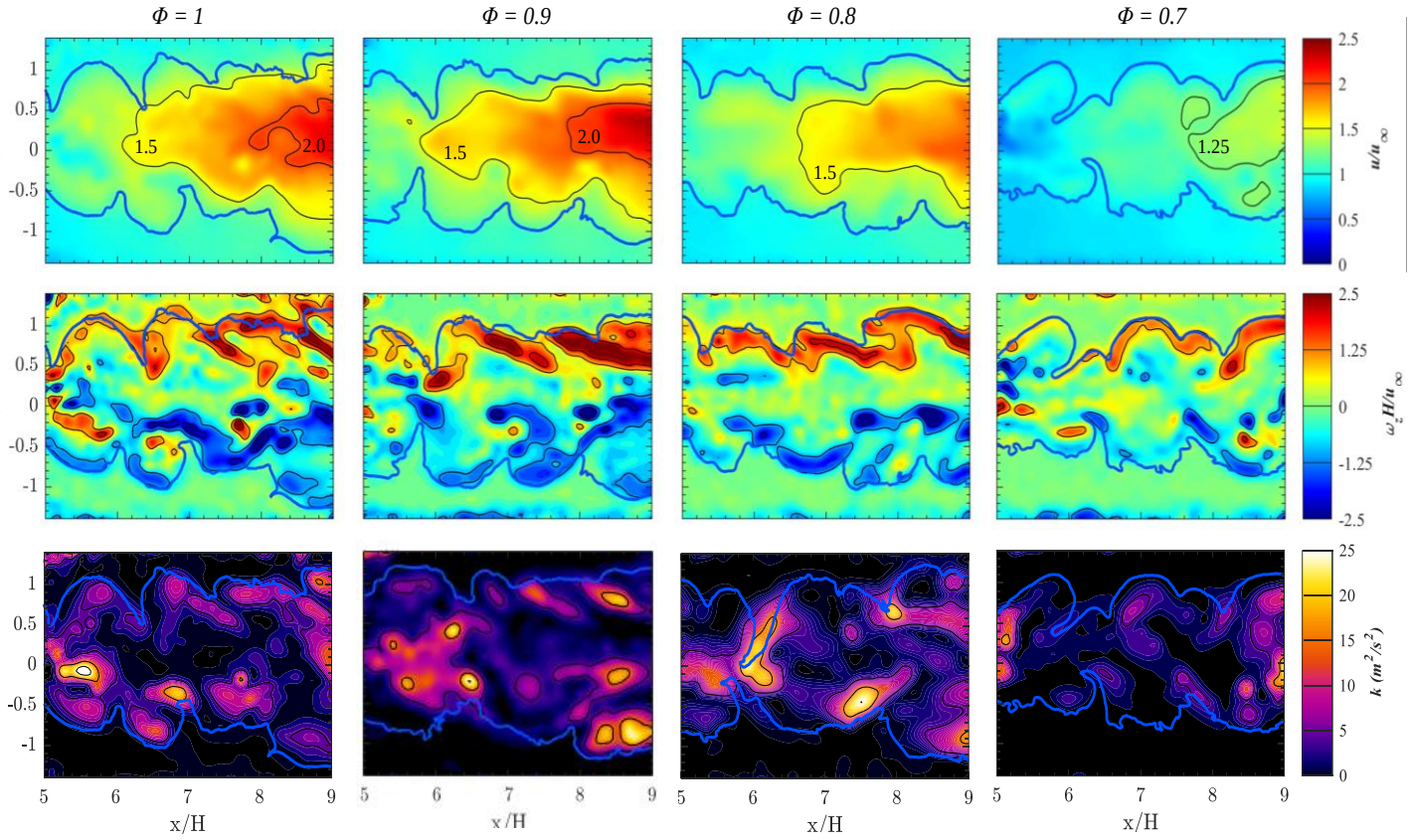

Figure 3: Instantaneous contours of streamwise velocity (u), spanwise vorticity (ωz), and turbulent kinetic energy (k) as a function of equivalence ratio (φ). The contours are superimposed with instantaneous flame front contours, depicted by the blue curves

Figure 3 shows several instantaneous flow contours as a function of equivalence ratio. The flame front is overlaid on each contour, shown as blue curves. The figure includes streamwise velocity, spanwise vorticity, and turbulent kinetic energy contours.

As shown in the top row of Fig. 3, the streamwise velocity increases with equivalence ratio due to the increased heat of combustion as Φ approaches 1. The increased heat release will lead to reduced flow densities, which causes the streamwise velocity to increase to satisfy mass continuity. The spanwise vorticity is largest at the instantaneous position of the flame. The vorticity also shows an increase in magnitude as the equivalence ratio increases. The strong vorticity present at the flame front is due to baroclinic torque, a vorticity source terms that arises in the vorticity transport equation, provided in tensor form in Eq. (6) [32,33]. Here, S_{ij} is the rate of strain tensor, τ_{ij} is the viscous stress tensor, defined as $\tau_{ij} = 2\mu S_{ij} - 0.67\mu S_{kk}\delta_{ij}$, δ_{ij} is the Kronecker delta function, and ε_{ijk} is the cyclic permutation tensor. Baroclinic torque is produced through the misalignment of the density and pressure gradients and is a significant term for confined reacting flows . As the equivalence ratio approaches $\Phi = 1.0$, the increased heat of combustion will cause the flow density to decrease and the streamwise velocity to increase. This will cause both the density gradient across the flame, as well as the mean pressure gradient in the flow field to increase in magnitude. Therefore, there is a greater production of vorticity from the baroclinic mechanism.

$$\frac{D\omega_i}{Dt} = \underbrace{S_{ij}\omega_j}_{stretching} - \underbrace{S_{jj}\omega_i}_{dilitation} + \underbrace{\frac{\epsilon_{ijk}}{\rho^2}\frac{\partial\rho}{\partial x_j}\frac{\partial P}{\partial x_k}}_{\substack{baroclinic \\ torque}} - \underbrace{\frac{\varepsilon_{ijk}}{\rho^2}\frac{\partial\rho}{\partial x_k}\frac{\partial\tau_{kl}}{\partial x_l}}_{\substack{viscous \\ torque}} + \underbrace{\nu\frac{\partial^2\omega_i}{\partial x_k^2}}_{\substack{viscous \\ diffusion}} \quad (6)$$

Turbulent kinetic energy contours for each equivalence ratio case are also provided in Fig. 3. It is observed that each case shows intense regions of turbulent kinetic energy (k) near the flame but concentrated toward the product region. It is noted that strong magnitudes of turbulent kinetic

energy are not correlated with strong magnitudes of vorticity. However, local magnitudes of k generally increase as the equivalence ratio increases.

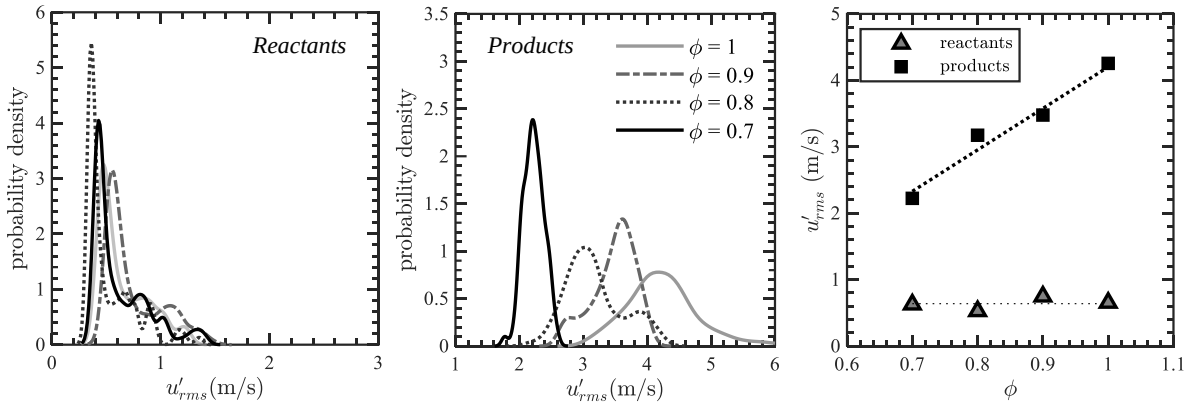

Figure 4: Probability density functions of u'_rms in the reactant and product regions, and the mean values of u'_rms as a function of equivalence ratio.

To better characterize the effects of heat release on turbulence production, Fig. 4 displays probability density functions of u′rms in both the reactant and product regions. The mean values were taken from a region in the reactants between x/H = 6.0 – 8.0 and y/H = 1.6 – 1.8 while the products were taken from x/H = 6.0 – 8.0 and y/H = 0 - 0.2. The mean values from the pdf are also displayed in Fig. 4. Although the turbulent fluctuations in the reactants are nominally constant, the products depict a linear increase as the equivalence ratio increases. This demonstrates that the magnitude of turbulent fluctuations produced by the flame are a function of the flame's heat release.

It is evident that there is an intensification of turbulence across a flame as the flow progresses from reactants to products. This conclusion contradicts classical literature and theories which have concluded that premixed flames dampen turbulence as the flow progresses from

reactants to products. The trend of increased turbulence intensities with the equivalence ratio is a result of the flame's heat release acting on a confined flow. Since the confined flow is not free to expand without physical boundaries, the addition of heat will inject kinetic energy into the flow. To provide a visual representation, a schematic of the conversion from thermal to mechanical energy is provided in Fig. 5. As previously mentioned, the increase in flow kinetic energy will primarily arise in the form of increased mean velocities. However, a portion of the kinetic energy will also be transferred to turbulence. The energy transferred to turbulence can manifest as either increased turbulence fluctuations or increased turbulence length scales. However, since the flow is confined, the length scales cannot grow unbounded, and thus a majority of the turbulent energy appears as increased turbulence fluctuations in the product region. These conclusions are validated by the current study, which also demonstrates that increasing the flame's heat release results in greater turbulence production by the flame. In contrast, unconfined reacting flow fields are unbounded, and thus the kinetic energy gained by the flow primarily results in flow expansion with decreased turbulence intensities.

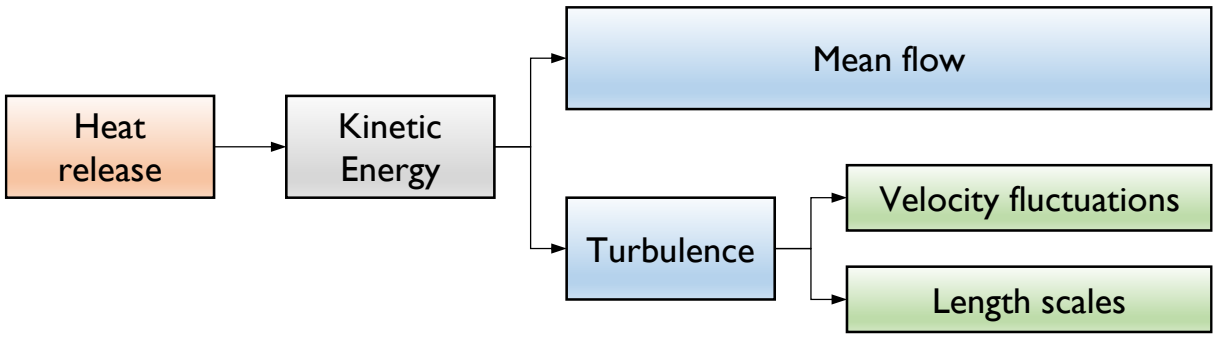

Figure 5: A schematic representation of the conversion from thermal to mechanical energy in confined reacting flows

Based on recent research by Rising et al.[34], the conclusions above will also uphold for a wide range of inlet turbulence intensities and are not limited to the conditions explored here. Using the same experimental facility, research from Rising et al. has shown that turbulence intensities will be augmented across a flame for inlet conditions up to u'rms/sl = 34.0 and Ka = 143.4. A comparison between the current turbulence conditions and the previous work is plotted on the premixed combustion regime diagram in Fig. 6. The combined conditions between both studies sweeps through the corrugated flamelet, thin reaction zone, and the lower portion of the broken/ distributed reaction regimes. Thus, the conversion from thermal to mechanical energy, and the augmentation of turbulence for confined flows should be upheld across a wide range of engine relevant conditions.

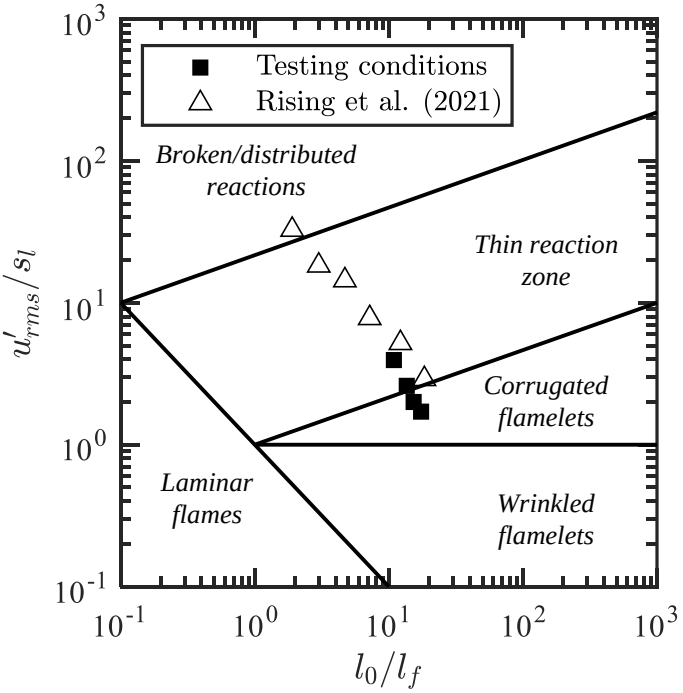

Figure 6: Test conditions plotted on the Borghi/Peters premixed combustion regime diagram along with data points from rising et al.

3.2 Turbulence Evolution in Extended Progress Variable Space

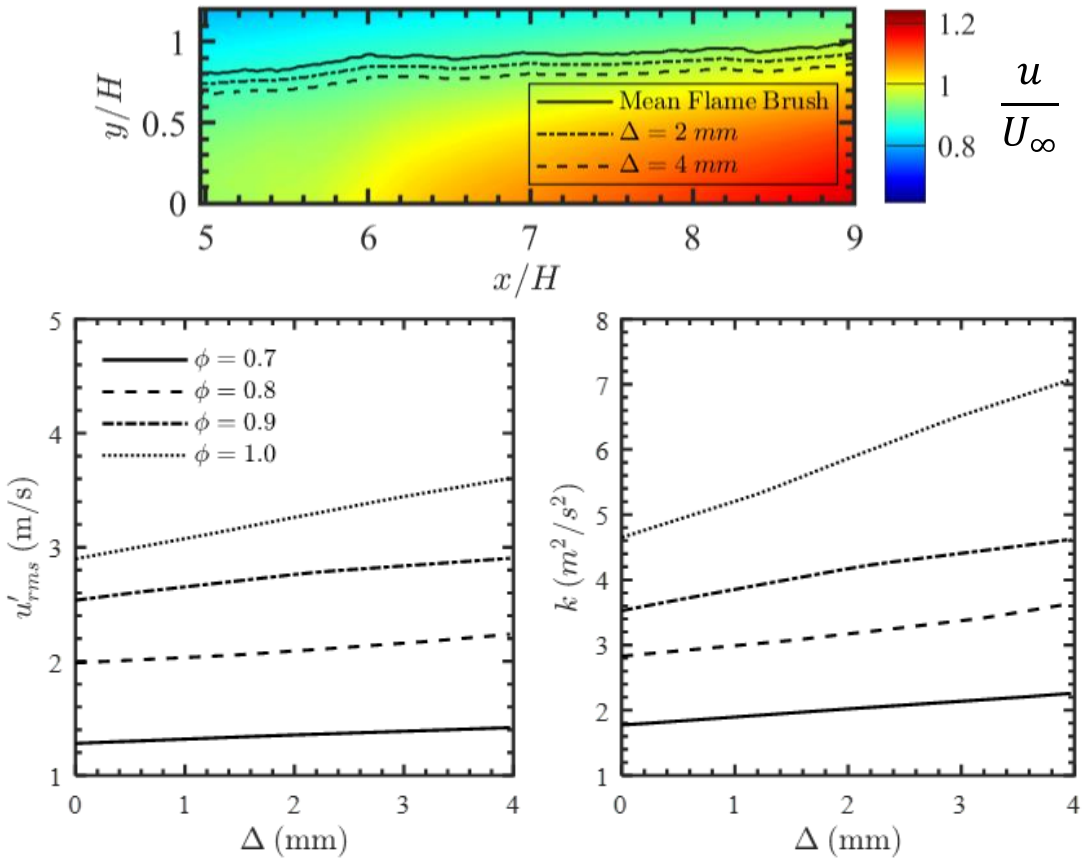

Figure 7: Spatial profiles of u'rms and turbulent kinetic energy in extended progress variable space.

To better characterize the spatial evolution of turbulence across confined premixed flames, an extended progress variable space, Δ, is defined. This extended progress variable starts from Δ = 0 mm, or the mean flame front, and proceeds in a direction normal to the flame front toward the product region. Figure 7 shows an example of the mean flame front, along with iso-contours of extended progress variable space. The iso-contours are overlayed onto the contour of mean streamwise velocity.

Turbulence fluctuations and turbulent kinetic energy are averaged along the extended progress variable iso-contours and displayed in Fig. 7. It's observed that for each of the cases, velocity fluctuations and turbulent kinetic energy monotonically increase over the progress variable space. The magnitude of turbulence fluctuations and turbulent kinetic energy increase with equivalence ratio.

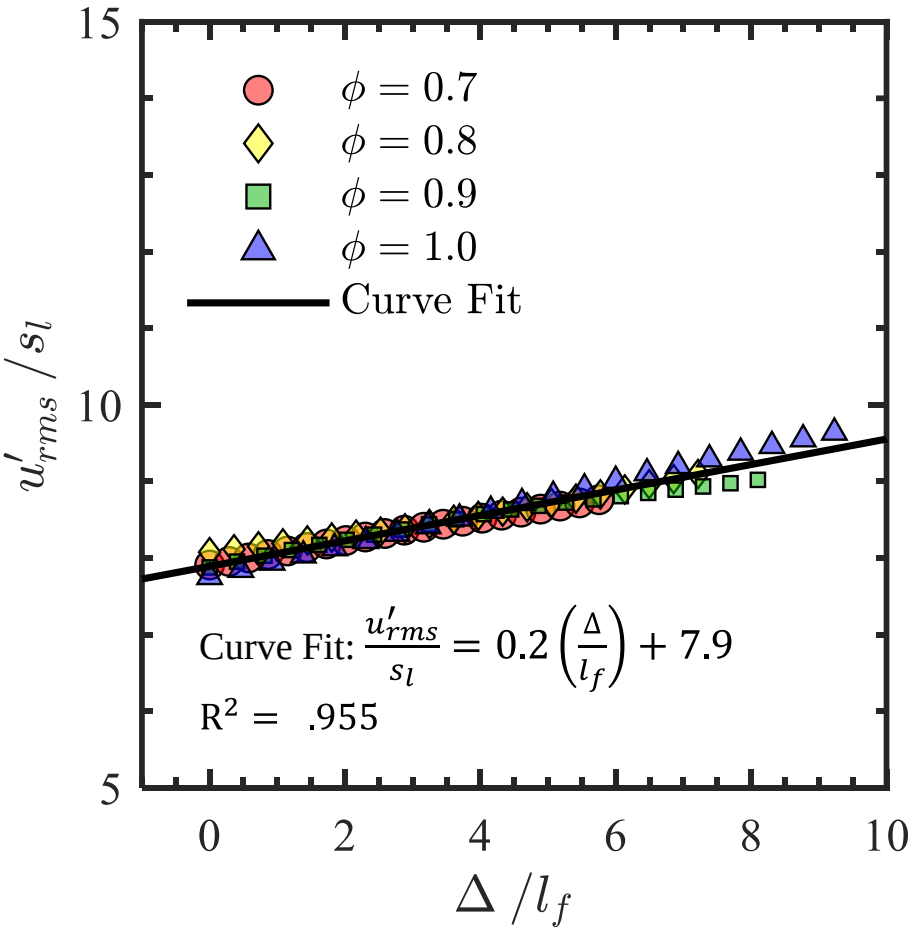

Figure 8: Nondimensional turbulence evolution in extended progress variable space and corresponding curve fit equation

Interestingly, a linear increase in u′rms and k as a function of equivalence ratio is observed in both Figs. 4 and 7. Thus, the question becomes: can the turbulence evolution across a flame be predicted based on flame scales or chemical heat release? Both flame speed and thickness are proportional to equivalence ratio, and thus are ideal scales to collapse the spatial profiles into a single curve. As such, the turbulence fluctuations from Fig. 7 are non-dimensionalized by the laminar flame speed, and the progress variable Δ is non-dimensionalized by the laminar flame thickness. The resulting non-dimensional curves are shown in Fig. 8 and nominally collapse on top of each other. Using a linear curve fit, the collapsed data fits the linear equation provided in Fig. 8 with an R2 = 0.96. This initial model indicates that augmented turbulence across a premixed flame may be predicted with flame scales or the corresponding heat of combustion.

3.3 RANS Decomposition

To better characterize heat release on flow dynamics, a decomposition of the Reynolds Averaged Navier Stokes (RANS) equation was performed. The RANS equation, neglecting body forces, is provided in Eq. (7). Each term was independently calculated in the reactant and product regions with the exception of the pressure term which was calculated by solving Eq. (7). The density and viscosity were assumed to be uniform in both the reactant and product regions, where each value was calculated using NASA's chemical equilibrium calculator. A mean value for each term was obtained by averaging the data in the freestream reactants between x/H = 6 - 8 and y/H = 1.6 – 1.8 and averaging the data in the products between x/H = 6-8 and y/H = 0 - 0.2.

$$\underbrace{\bar{u}_j \frac{\partial \bar{u}_i}{\partial x_j}}_{\substack{mean \\ advection}} = \underbrace{-\frac{1}{\rho}\frac{\partial \bar{p}}{\partial x_i}}_{\substack{pressure \\ gradient}} + \underbrace{\nu \frac{\partial^2 \bar{u}_i}{\partial x_j \partial x_j}}_{\substack{viscous \\ stress}} - \underbrace{\frac{\partial \overline{u_i' u_j'}}{\partial x_j}}_{\substack{turbulent \\ stress}} \tag{7}$$

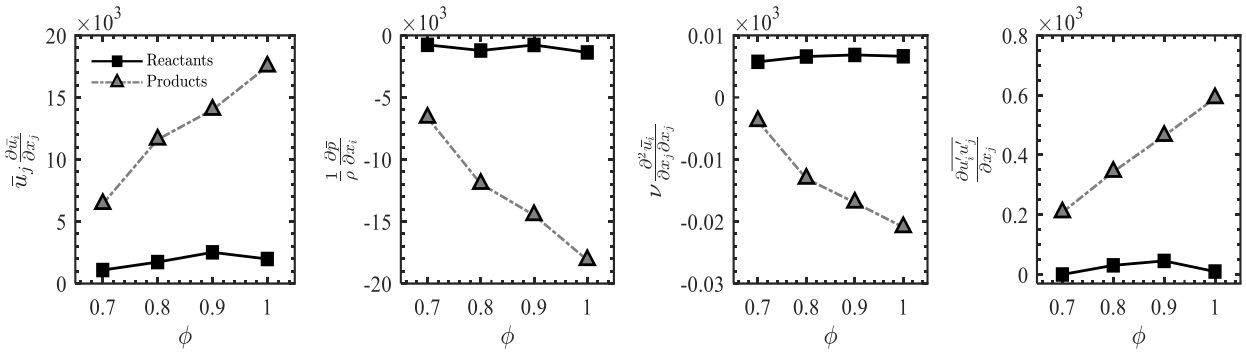

Figure 9: RANS decomposition in the reactant and product regions

The mean value for each RANS term is presented in Fig. 9. For each term, the magnitude remains nominally constant in the reactants for each equivalence ratio. The progression from reactants to products augments all terms and each term's magnitude increases with equivalence ratio. As previously shown, increasing equivalence ratio produces higher streamwise velocity, resulting in stronger mean advection. The advection term is naturally coupled with an increased favorable pressure gradient which is also observed in Fig. 9. Both the viscous stress and turbulent stress terms also increase in magnitude as the equivalence ratio increases. The viscous stress term is 2-3 orders of magnitude smaller than the mean advection and pressure gradient terms and is therefore not a significant contributor to momentum transport in the confined reacting flow. The turbulent stress term, however, is an order of magnitude larger than the viscous stress term. Thus, turbulence produced from mean flow shear and heat driven flow acceleration (dilatation) should overshadow viscous dampening. Thus, turbulence is not dampened across the premixed flame and is sustained by mean advection in a confined reacting flow with mean pressure gradients.

CHAPTER FOUR: CONCLUSIONS

The effects of heat release and flame scales on turbulence evolution across confined premixed flames was investigated in a bluff-body combustor. Both Particle Image Velocimetry (PIV) and CH* chemiluminescence imaging were utilized to obtain detailed flow field measurements and flame front topology, respectively. Several heat release conditions were tested which were chosen by increasing the equivalence ratio from 0.7 to 1.0.

Contrary to other literature stating premixed flames typically dampen turbulence, the experiment showed that for a confined premixed flame, turbulence is augmented across the flame due to heat release and confinement effects. For all cases, the conversion from thermal energy to kinetic energy contributes to an increase in turbulent kinetic energy. Since the flow is confined and not free to expand, the increase in turbulent kinetic energy primarily arises as increased velocity fluctuations rather than increased turbulence length scales. Furthermore, increasing the heat release through the equivalence ratio was shown to increase the turbulence production.

An extended progress variable, Δ, was defined to further characterize the spatial evolution of turbulence across the premixed flame. The results showed a monotonic increase in turbulence intensity as the flow evolved from reactants to products, with the magnitudes of u'_{rms} and turbulent kinetic energy increasing with the equivalence ratio. Nondimensionalizing the spatial evolution profiles by the laminar flame scales was shown to collapse the curves, and a unified correlation was developed. The correlation provides evidence that the augmented turbulence is directly correlated with the flame's heat release and can provide a foundation to better predict turbulence dynamics in confined premixed flows.

A RANS decomposition was also performed to better understand the effects of heat release on flow dynamics. The decomposition showed the advective and pressure terms were dominant over the stress terms for every test condition. For all cases, the viscous stress term maintained the smallest order of magnitude and is not expected to play a significant role in turbulent flow transport. However, it was noted that the turbulent stress term was an order of magnitude larger than the viscous term. The results suggest that flame-generated turbulence can be sustained in confined premixed flows due to mean advection and pressure gradients.

These conclusions provide a new perspective on turbulence-heat release interactions and confirm that the typical kinematic descriptions for turbulence evolution do not necessarily hold true across confined premixed flames. Based on recent existing literature, the trends presented here should also uphold for a wide range of turbulence conditions, up to and exceeding Ka = 100. The results can guide new predictive tools for spatial turbulence evolution that can aid future modeling and design efforts, leading to more efficient propulsion and power engines.

REFERENCES

[1] Steinberg, A. M., Hamlington, P. E., and Zhao, X., 2021, "Structure and Dynamics of Highly Turbulent Premixed Combustion," Progress in Energy and Combustion Science, **85**, p. 100900.

[2] Chakraborty, N., Katragadda, M., and Cant, R. S., 2011, "Statistics and Modelling of Turbulent Kinetic Energy Transport in Different Regimes of Premixed Combustion," Flow Turbulence Combust, **87**(2), pp. 205–235.

[3] Wang, Z., and Abraham, J., 2017, "Effects of Karlovitz Number on Turbulent Kinetic Energy Transport in Turbulent Lean Premixed Methane/Air Flames," Physics of Fluids, **29**(8), p. 085102.

[4] MacArt, J. F., Grenga, T., and Mueller, M. E., 2019, "Evolution of Flame-Conditioned Velocity Statistics in Turbulent Premixed Jet Flames at Low and High Karlovitz Numbers," Proceedings of the Combustion Institute, **37**(2), pp. 2503–2510.

[5] MacArt, J. F., Grenga, T., and Mueller, M. E., 2018, "Effects of Combustion Heat Release on Velocity and Scalar Statistics in Turbulent Premixed Jet Flames at Low and High Karlovitz Numbers," Combustion and Flame, **191**, pp. 468–485.

[6] Lee, J., MacArt, J. F., and Mueller, M. E., 2020, "Heat Release Effects on the Reynolds Stress Budgets in Turbulent Premixed Jet Flames at Low and High Karlovitz Numbers," Combustion and Flame, **216**, pp. 1–8.

[7] Wang, H., Hawkes, E. R., Savard, B., and Chen, J. H., 2018, "Direct Numerical Simulation of a High Ka CH4/Air Stratified Premixed Jet Flame," Combustion and Flame, **193**, pp. 229–245.

[8] Hamlington, P. E., Poludnenko, A. Y., and Oran, E. S., 2011, “Interactions between Turbulence and Flames in Premixed Reacting Flows,” Phys. Fluids, **23**(12), p. 125111.

[9] Chakraborty, N., 2021, “Influence of Thermal Expansion on Fluid Dynamics of Turbulent Premixed Combustion and Its Modelling Implications,” Flow Turbulence Combust, **106**(3), pp. 753–848.

[10] Darragh, R., Towery, C. A. Z., Meehan, M. A., and Hamlington, P. E., 2021, “Lagrangian Analysis of Enstrophy Dynamics in a Highly Turbulent Premixed Flame,” Physics of Fluids, **33**(5), p. 055120.

[11] Su, Y., 2022, “Suppression of the Turbulent Kinetic Energy and Enhancement of the Flame-Normal Reynolds Stress in Premixed Jet Flames at Small Lewis Numbers,” Combustion and Flame, **246**, p. 112461.

[12] Wabel, T. M., Skiba, A. W., and Driscoll, J. F., 2018, “Evolution of Turbulence through a Broadened Preheat Zone in a Premixed Piloted Bunsen Flame from Conditionally-Averaged Velocity Measurements,” Combustion and Flame, **188**, pp. 13–27.

[13] Skiba, A. W., Carter, C. D., Hammack, S. D., Miller, J. D., Gord, J. R., and Driscoll, J. F., 2019, “The Influence of Large Eddies on the Structure of Turbulent Premixed Flames Characterized with Stereo-PIV and Multi-Species PLIF at 20 kHz,” Proceedings of the Combustion Institute, **37**(2), pp. 2477–2484.

[14] Kazbekov, A., and Steinberg, A. M., 2021, “Physical Space Analysis of Cross-Scale Turbulent Kinetic Energy Transfer in Premixed Swirl Flames,” Combustion and Flame, **229**, p. 111403.

[15] Kazbekov, A., Kumashiro, K., and Steinberg, A. M., 2019, “Enstrophy Transport in Swirl Combustion,” Journal of Fluid Mechanics, **876**, pp. 715–732.

[16] Geikie, M. K., and Ahmed, K. A., 2018, "Pressure-Gradient Tailoring Effects on the Turbulent Flame-Vortex Dynamics of Bluff-Body Premixed Flames," Combustion and Flame, **197**, pp. 227–242.

[17] Geikie, M. K., Rising, C. J., Morales, A. J., and Ahmed, K. A., 2021, "Turbulent Flame-Vortex Dynamics of Bluff-Body Premixed Flames," Combustion and Flame, **223**, pp. 28–41.

[18] Geikie, M. K., Carr, Z. R., A. Ahmed, K., and Forliti, D. J., 2017, "On the Flame-Generated Vorticity Dynamics of Bluff-Body-Stabilized Premixed Flames," Flow Turbulence Combust, **99**(2), pp. 487–509.

[19] Whitman, S. H. R., Souders, T. J., Meehan, M. A., Brasseur, J. G., and Hamlington, P. E., 2022, "Pressure Gradient Tailoring Effects on Vorticity Dynamics in the Near-Wake of Bluff-Body Premixed Flames," Proceedings of the Combustion Institute.

[20] Morales, A. J., Thornton, M., Tonarely, T. G. M., and Ahmed, K. A., 2022, "The Role of Flow Confinement on Turbulent Kinetic Energy Transfer across Premixed Flames," Combustion and Flame, **241**, p. 112103.

[21] Morales, A. J., Lasky, I. M., Geikie, M. K., Engelmann, C. A., and Ahmed, K. A., 2019, "Mechanisms of Flame Extinction and Lean Blowout of Bluff Body Stabilized Flames," Combustion and Flame, **203**, pp. 31–45.

[22] Morales, A. J., Reyes, J., Joo, P. H., Boxx, I., and Ahmed, K. A., 2020, "Pressure Gradient Tailoring Effects on the Mechanisms of Bluff-Body Flame Extinction," Combustion and Flame, **215**, pp. 224–237.

[23] Pfadler, S., Beyrau, F., and Leipertz, A., 2007, "Flame Front Detection and Characterization Using Conditioned Particle Image Velocimetry (CPIV)," Opt. Express, OE, **15**(23), pp. 15444–15456.

[24] Zheng, Y., Weller, L., and Hochgreb, S., 2022, "Instantaneous Flame Front Identification by Mie Scattering vs. OH PLIF in Low Turbulence Bunsen Flame," Exp Fluids, **63**(5), p. 79.

[25] Osborne, J. R., Ramji, S. A., Carter, C. D., Peltier, S., Hammack, S., Lee, T., and Steinberg, A. M., 2016, "Simultaneous 10 KHz TPIV, OH PLIF, and CH2O PLIF Measurements of Turbulent Flame Structure and Dynamics," Exp Fluids, **57**(5), p. 65.

[26] Otsu, N., 1979, "A Threshold Selection Method from Gray-Level Histograms," IEEE Transactions on Systems, Man, and Cybernetics, **9**(1), pp. 62–66.

[27] Moore, G. A., 1968, "Automatic Scanning and Computer Processes for the Quantative Analysis of Micrographs and Equivalent Subjects," Pictorial Pattern Recognition, pp. 275–362.

[28] Lafay, Y., Renou, B., Leventiu, C., Cabot, G., and Boukhalfa, A., 2009, "Thermal Structure of Laminar Methane/Air Flames: Influence of H2 Enrichment and Reactants Preheating," Combustion Science and Technology, **181**(9), pp. 1145–1163.

[29] Vagelopoulos, C. M., Egolfopoulos, F. N., and Law, C. K., 1994, "Further Considerations on the Determination of Laminar Flame Speeds with the Counterflow Twin-Flame Technique," Symposium (International) on Combustion, **25**(1), pp. 1341–1347.

[30] Amirante, R., Distaso, E., Tamburrano, P., and Reitz, R. D., 2017, "Laminar Flame Speed Correlations for Methane, Ethane, Propane and Their Mixtures, and Natural Gas and Gasoline for Spark-Ignition Engine Simulations," International Journal of Engine Research, **18**(9), pp. 951–970.

[31] Welch, P., 1967, "The Use of Fast Fourier Transform for the Estimation of Power Spectra: A Method Based on Time Averaging over Short, Modified Periodograms," IEEE Transactions on Audio and Electroacoustics, **15**(2), pp. 70–73.

[32] Dopazo, C., Cifuentes, L., Alwazzan, D., and Chakraborty, N., 2018, "Influence of the Lewis Number on Effective Strain Rates in Weakly Turbulent Premixed Combustion," Combustion Science and Technology, **190**(4), pp. 591–614.

[33] Lipatnikov, A. N., Nishiki, S., and Hasegawa, T., 2014, "A Direct Numerical Simulation Study of Vorticity Transformation in Weakly Turbulent Premixed Flames," Physics of Fluids, **26**(10), p. 105104.

[34] Rising, C. J., Morales, A. J., Geikie, M. K., and Ahmed, K. A., 2021, "The Effects of Turbulence and Pressure Gradients on Vorticity Transport in Premixed Bluff-Body Flames," Physics of Fluids, **33**(1), p. 017106.